The Crystal Structure of the Human Titin: Obscurin Complex Reveals a Conserved yet Specific Muscle M-Band Zipper Module

Stefano Pernigo[1], Atsushi Fukuzawa[1,2], Alessandro Pandini[1,3], Mark Holt[1,2], Jens Kleinjung[4], Mathias Gautel[1,2] and Roberto A. Steiner[1]

1 - *Randall Division of Cell and Molecular Biophysics,* King's College London, New Hunt's House, Guy's Campus, London SE1 1UL, UK
2 - *Cardiovascular Division,* King's College London, New Hunt's House, Guy's Campus, London SE1 1UL, UK
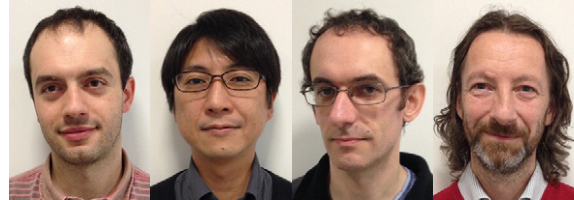3 - *Department of Computer Science and Synthetic Biology Theme–Brunel University London,* Uxbridge UB8 3PH, UK
4 - *Division of Mathematical Biology,* MRC National Institute for Medical Research, The Ridgeway, London NW7 1AA, UK

Correspondence to Roberto A. Steiner:
roberto.steiner@kcl.ac.uk
http://dx.doi.org/10.1016/j.jmb.2014.11.019
Edited by J. Sellers

Stefano Pernigo, Atsushi Fukuzawa, Alessandro Pandini and Mark Holt

Abstract

M10 is the most C-terminal immunoglobulin (Ig) domain of the giant protein titin and a frequent target of disease-linked mutations. Currently, it is the only known muscle Ig domain able to interact with two alternative ligands—obscurin and obscurin-like-1 (Obsl1)—in different sarcomeric subregions. Obscurin and Obsl1 use their homologous N-terminal Ig domain (O1 in obscurin and OL1 in Obsl1) to bind M10 in a mutually exclusive manner. We present here the X-ray structure of the human titin:obscurin M10:O1 complex extending our previous work on the M10:OL1 interaction. Similar to M10:OL1, the M10:O1 complex displays a chevron-shaped antiparallel Ig–Ig architecture held together by a conserved molecular interface, which we validated by isothermal titration calorimetry and sorting experiments in neonatal rat cardiomyocytes. O1, although structurally related to OL1 and M10, both members of the intermediate set (I-set) Ig family, presents an intriguing switch of its βA' strand. This leads to structural differences between the complexes, particularly for the "open side" of the chevron-shaped assembly. A bioinformatics analysis reveals that the βA'-switch observed for O1 is rare and that it is involved in mediating protein–protein interactions. Molecular dynamics simulations also suggest that this topological alteration substantially increases local flexibility compared to the conventional I-set Ig domains. The O1/OL1 Ig domains are candidate discriminatory structural modules potentially directing the binding of specific additional partners at the M-band. Cellular sorting experiments in neonatal rat cardiomyocytes are consistent with the view that the
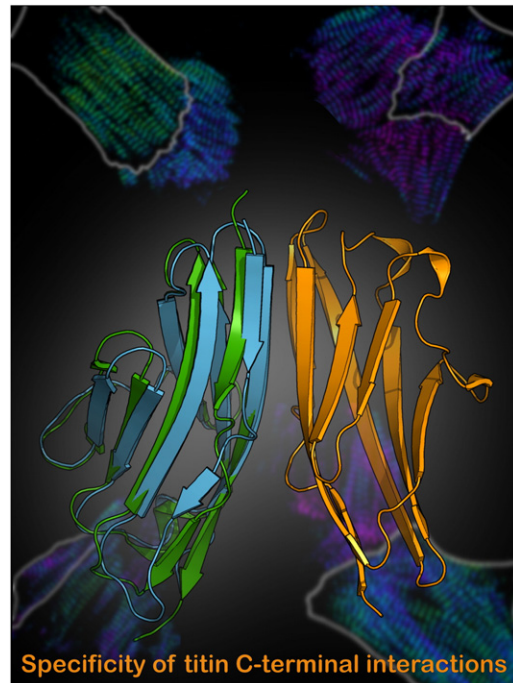
Legend: The C-terminus of the giant muscle protein titin binds obscurin at the myofibrillar periphery and obscurin-like-1 at the myofibrillar core. The crystal structure of the titin:obscurin complex reveals a conserved zipper module and an unconventional topology for the obscurin immunoglobulin domain. The titin:obscurin/obscurin-like-1 complexes appear perfectly poised as discriminatory structural elements potentially directing the binding of additional partners.

titin:obscurin/Obsl1 complexes might be a platform for higher-order interactions.

Introduction

The assembly and maintenance of functional sarcomeres in cardiac and skeletal muscles rely on the establishment of complex multiprotein networks regulated both spatially and temporally [1]. The giant protein titin spanning half of the sarcomere length offers a docking platform for several binding partners. At the M-band, the C-terminus of titin is engaged in a complex with the 800-kDa protein obscurin or, alternatively, its smaller 130- to 230-kDa obscurin-like-1 (Obsl1) analogue (Fig. 1a) [2]. Obscurin and Obsl1, in turn, interact with the myosin cross-linking protein myomesin, a critical component of M-band structural integrity [2]. Titin's C-terminus is important for muscle function as multiple mutations mapping to this region cause hereditary myopathies such as tibial muscular dystrophy and limb girdle muscular dystrophy 2J [3,4]. Cellular roles for obscurin and Obsl1 are slowly emerging. Like titin and other sarcomeric proteins, obscurin and Obsl1 share a common immunoglobulin (Ig)-rich modular structure, which, in the case of obscurin, is more extended, featuring additional signaling and protein-binding domains absent in Obsl1 (Fig. 1a) [2]. The presence of a nonmodular C-terminus able to interact with sAnk1.5 (small ankyrin-1 isoform 5) and Ank2 (ankyrin-2) led to the suggestion that obscurin plays a role in establishing the sarcomere–sarcoplasmic reticulum (SR) connection [5,6]. Experiments in $Obscn^{-/-}$ mice support this view. Ablation of the $Obscn$ gene results in changes in longitudinal SR architecture with alterations in several SR or SR-associated proteins, such as Ank2 and β-spectrin, as well as disruption of sAnk1.5 expression and localization [7,8]. Similarly, depletion of obscurin in zebrafish led to disturbances in the extracellular matrix organization during skeletal muscle development [9]. Signaling roles for obscurin, in addition to structural ones, are suggested by the presence of an SH3–DH–PH domain tandem predicted to act as guanine nucleotide GDP–GTP exchange factors, as well as up to two kinase domains present in some of its isoforms [10]. From a pathological viewpoint, $OBSCN$ polymorphisms in humans have been linked to the development of hypertrophic cardiomyopathy [11] as well as to aspirin hypersensitivity in asthmatics [12]. The latter effect can be rationalized considering the interplay between airway remodeling and intracellular Ca^{2+} regulation by the SR of the airway smooth muscle cells; however, functional evidence for the pathogenicity of these variants at the biochemical level is lacking.

Obsl1 lacks the Ank-binding sites that link the obscurin C-terminus to the SR. In keeping with this,

Obsl1 and obscurin exhibit alternative subcellular localization in the muscle [2]. While obscurin is found at the myofibril periphery, Obsl1 localizes in the myofibril core where it likely acts as an adaptor molecule. Recently, mutations in Obsl1 have been linked to the rare hereditary growth retardation 3-M syndrome [13] with a role for Obsl1 in the maintenance of cullin-7 levels [14] and regulation of insulin-like growth factor binding proteins [13]. Pathogenic cullin-7 mutations are known as the primary cause of 3-M syndrome [15]. A recent account further strengthens the link between Obsl1 and cullin-7 by showing that these proteins physically interact in neurons and that Obsl1 plays a role in Golgi morphogenesis and dendrite elaboration [16]. Overall, in spite of similar modular architectures, obscurin and Obsl1 appear to have rather distinct biological functions.

At the molecular level, obscurin and Obsl1 are targeted to the muscle M-band by an interaction of their first Ig domain (hereafter O1 and OL1, respectively) with the most C-terminal titin's Ig domain (M10) as well as by an interaction of their third Ig domain (O3 and OL3) with myomesin [2] (Fig. 1a). The atomic basis for the M10:OL1 interaction has recently been elucidated by us and others [17,18]. The complex displays a novel chevron-shaped architecture with an antiparallel arrangement of its Ig protomers in agreement with the orientation expected in the sarcomere. We have extended our previous structural work on M10:OL1 and present here the X-ray structure of the human titin:obscurin M10:O1 complex in two alternative crystal forms. In spite of a largely conserved binding interface, an uncommon topological variation in the O1 module leads to structural differences between the M10:O1 and M10:OL1 complexes, particularly for the "open side" of their "chevron-shaped" architecture. The O1 and OL1 modules appear perfectly poised as discriminatory structural elements potentially involved in the binding of additional specific partners.

Results and Discussion

Structure solution of the M10:O1 complex

The initial design of the M10:O1 constructs for crystallographic studies was guided by the titin:Obsl1 M10:OL1 structure [17]. *In vitro* reconstituted $M10^{1-99}$:$O1^{7-109}$ ($M10^{1-99}$ corresponds to titin$^{34252-34350}$; $O1^{7-109}$ is Obscurin$^{7-109}$) failed however to crystallize. Partial degradation of $O1^{7-109}$ appeared a
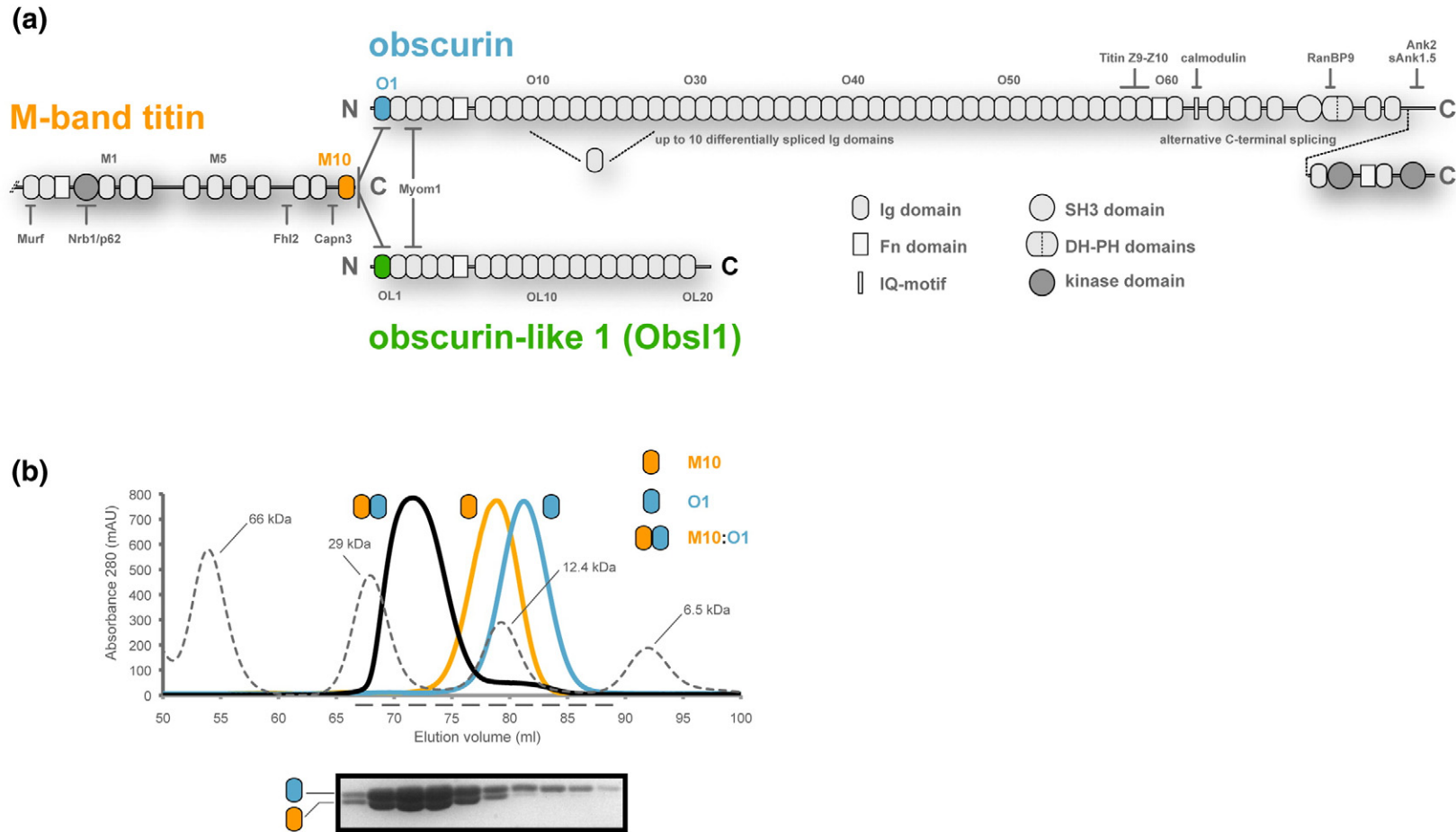
Fig. 1. Titin's C-terminus interacts with obscurin/Obsl1 N-terminus. (a) Cartoon representation of the modular organization of M-band titin and its obscurin and Obsl1 binding partners. The C-terminal M10 Ig domain of titin (shown in orange) interacts with the first Ig domain of obscurin (O1 in blue) and the first Ig domain of Obsl1 (OL1 in green) in a mutually exclusive fashion in different sarcomeric subregions. (b) SEC profile and SDS-PAGE analysis of the *in vitro* reconstituted M10:O1 complex.

Table 1. Data collection and refinement statistics

Data set	M10:O1 (trigonal)	M10:O1 (orthorhombic)
Data collection		
Beamline	I24 (DLS)	I24 (DLS)
Wavelength (Å)	0.9778	0.9686
Resolution range (Å)	40.0–3.30	35.70–1.95
Highest-resolution bin (Å)	(3.48–3.30)	(2.00–1.95)
Space group	$P3_221$	$P2_12_12_1$
Cell dimensions		
a, b, c (Å)	201.55, 201.55, 183.96	40.94, 66.88, 72.93
α, β, γ (°)	90, 90, 120	90, 90, 90
Unique reflections	64,369 (9315)	15,005 (1053)
Overall redundancy	3.0 (3.0)	3.3 (3.1)
Completeness (%)	98.9 (99.2)	99.0 (98.5)
R_{merge} (%)	21.5 (52.4)	5.3 (62.2)
$\langle I/\sigma(I) \rangle$	4.3 (2.2)	12.8 (2.0)
Refinement		
PDB code	4UOW	4C4K
R_{factor} (%)/R_{free} (%)	17.7/21.0	17.1/21.0
No. of non-H atoms		
Protein	25,784	1456
Heterogen (nonwater)	9	52
Water	0	114
rms bond lengths (Å)	0.008	0.010
rms bond angles (°)	1.00	1.12

possible reason for this (Fig. S1). We thus generated shorter O1[7–99] and O1[7–103] constructs for crystallization trials. Size-exclusion chromatography (SEC) shows that all *in vitro* reconstituted complexes elute earlier than the single components at a volume corresponding to a calculated molecular mass of about 20 kDa indicative of the formation of heterodimers in solution (Fig. 1b). Crystals of M10[1–99]:O1[7–99] and M10[1–99]:O1[7–103] were obtained as described in Materials and Methods. M10[1–99]:O1[7–103] crystallizes in the orthorhombic space group $P2_12_12_1$ with a single heterodimer in the asymmetric unit (a.u.). These crystals diffract to 1.95 Å resolution using synchrotron radiation. M10[1–99]:O1[7–99] crystals belong to the trigonal space group $P3_22_12$ and diffract to 3.30 Å resolution with 18 heterodimers in the a.u. Data processing and refinement statistics are shown in Table 1.

The structure of the M10:O1 complex in both space groups was solved by the molecular replacement technique. The final models for the low-resolution trigonal form and for the high-resolution orthorhombic form are characterized by R/R_{free} values of 17.7%/21.0% and 17.1%/21.0%, respectively. Electron density is observed for residues M10[2–98]:O1[7–100] and M10[2–98]:O1[7–99] in the orthorhombic and trigonal space groups, respectively. The lack of visible electron density after residue Asp[100] in the longer O1 construct suggests C-terminal flexibility in agreement with its tendency to natural proteolysis (Fig. S1). Although diffraction data in the $P3_22_12$ space group extend only to 3.3 Å resolution, noncrystallographic symmetry (NCS) averaging affords electron density maps of very good quality thanks to the presence of 18 copies of the complex in the a.u. (Fig. S2).

Overall architecture of the M10:O1 complex

The overall structure of the M10:O1 complex is shown in Fig. 2a and b. Given the higher resolution of the orthorhombic form, we will use this structure for the general description of the complex. M10 and O1 Ig domains are arranged head to tail with the N-terminal portion of M10 interacting with the C-terminal region of

Fig. 2. M10:O1 complex. (a and b) Cartoon representation of the M10:O1 complex viewed from the front and from the top, respectively. M10 is shown in orange. O1 is shown in blue. Secondary structural elements are labeled following the conventional nomenclature for Ig domains [21]. (c) Enlarged view of the boxed region in panel a highlighting important M10–O1 interactions. Color coding for carbon atoms is orange and blue for M10 and OL1, respectively; nitrogen, dark blue; oxygen, red. Hydrogen bonds and salt bridges are dotted green and red lines, respectively. (d) Sequence and secondary structure of the M10 and O1 domains. The sequence and secondary structure of the OL1 domain is also shown for comparison. Amino acids are color coded according to sequence conservation as highlighted by the conservation bar. Colored circles show residues of one domain contacting the other as indicated in the inset.
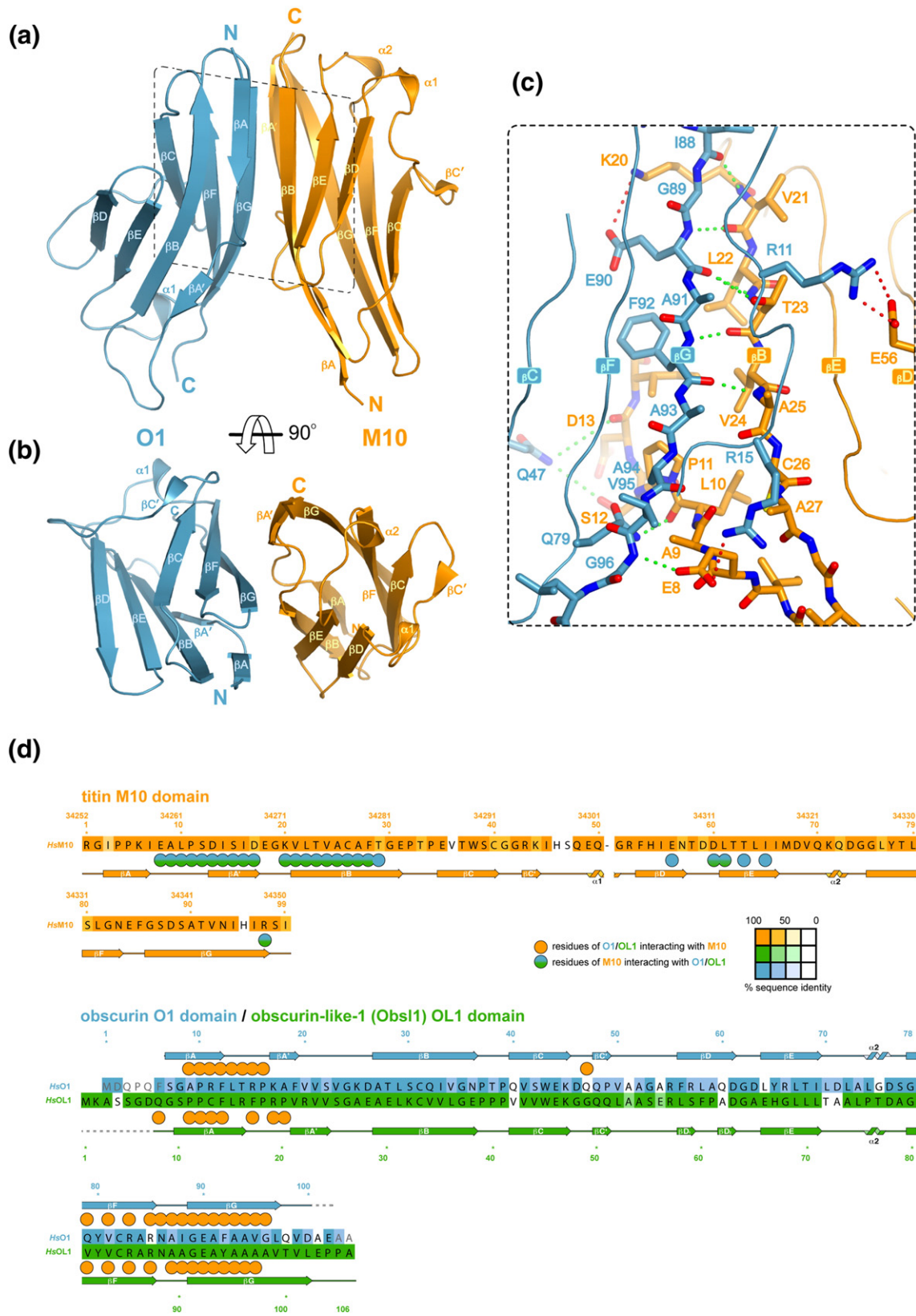
Fig. 2 (*legend on previous page*)

O1, giving rise to a complex stabilized by parallel intermolecular β-sheet augmentation. This architecture was seen for the first time for the M10:OL1 complex [17,18] and reflects the directionality of these filaments in the muscle M-band [19]. Owing to the parallel orientation of the long curved βB and βG strands in M10 and O1, respectively, the complex assumes a characteristic chevron shape (Fig. 2a). Five main-chain hydrogen bonds between residues V21, T23, and A25 of M10 βB and residues I88, E90, and F92 of O1 βG hold the initial portion of these strands together

(Fig. 2c), thus establishing an extended mixed inter-molecular β-sheet contributed by M10 (βA–βB–βE–βD) and O1 (βG–βF–βC–βC′), respectively. Additional H-bond interactions involve the M10 region connecting βB to βA′, which binds to residues belonging to βC, βF, and βG O1 strands. Salt bridges further hold the complex together: the carboxylate groups of M10[E8] and M10[E56] interact with the guanidinium groups of O1[R15] and O1[R11], respectively. Also, the side chain M10[K20] binds to the carboxylate of O1[E90]. Several hydrophobic interactions also stabilize the M10:O1
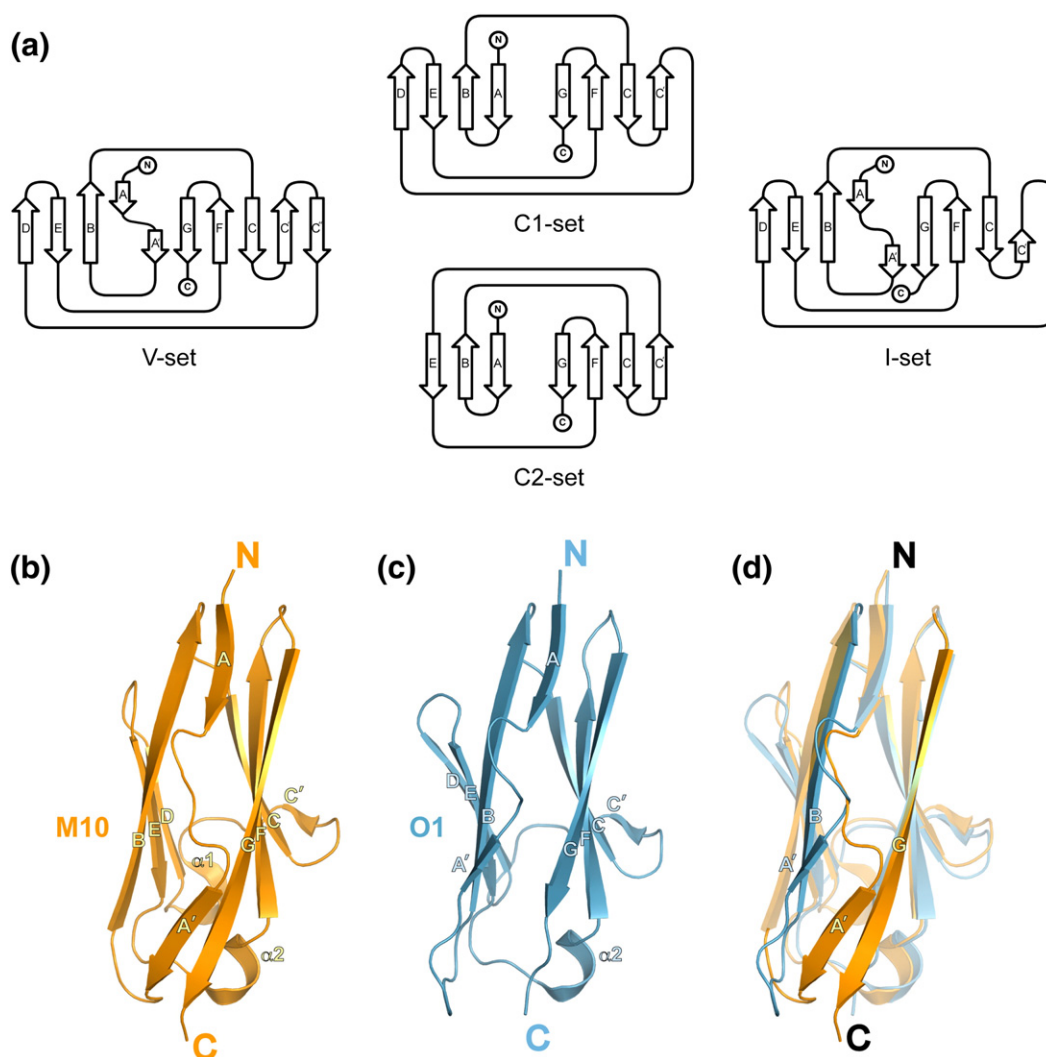
Fig. 3. Structure and topology of the M10 and O1 Ig-fold protomers. (a) Topology diagrams of variable (V-set), constant (C1-set and C2-set), and intermediate (I-set) Ig-fold domains. The I-set combines features of both the V-set and C1-set [20,21]. Strands are labeled according to the classical Ig-fold nomenclature. (b and c) Cartoon representation of M10 and O1, respectively. The common orientation highlights the two Ig-fold β-sheets facing each other. While M10 conforms to the typical I-set topology, O1 displays a repositioning of its βA′ strand. Strands are labeled as in panel a. M10 features two additional short α-helices (α1 and α2). Only the latter is present in O1. (d) Superposition of M10 and O1 highlighting the βAA′ linker, the βA′ strand, and the strand to which the latter H-bonds. Other parts of the Ig fold are shown as transparent cartoons. Letters N and C in panels b–d indicate the N- and C- termini, respectively.

complex as seen in the residue interaction scheme in Fig. 2d. Overall, the interface buries an area of about 1500 Å^2.

## The O1 domain is a deviant intermediate set Ig-fold

The intermediate set (I-set) subfamily of the Ig-fold is often found in muscle proteins [20]. This set was identified by Harpaz and Chothia [21] as a separate group distinct from the variable-like (V-set) and constant-like (C1- and C2-set) Ig domains and combining elements of both (Fig. 3a). Its topology consists of a total of nine strands arranged into two distinct β-sheets (βA–βB–βE–βD and βA′–βG–βF–βC–βC′) folded into a β-sandwich. Like the V-set, the I-set features a discontinuous first βA/βA′ strand distributed over both β-sheets. The βA strand is initially H-bonded to the βB strand in an antiparallel fashion contributing to the βA–βB–βE–βD sheet. Following a short break, it then crosses over to the other β-sheet where βA′ hydrogen bonds to the βG strand in a parallel arrangement forming one edge of the βA′–βG–βF–βC–βC′ sheet. The βA′ strand is not present in C1- and C2-sets. Also, I-set domains, like V-set domains, display conserved conformations for the links joining βA′ and βB strands as well as βE and βF strands

[21]. These loops are variable in C-sets. On the other hand, like the C1-set, the I-set lacks the βC″ strand typical of the V-set and features a very short βC′ strand.

M10 and O1 are structurally similar (Fig. 3b–d). They display an rmsd of 1.71 Å for 90 aligned C$^\alpha$ atoms. However, whereas M10 strictly conforms to the classical I-set topology (Fig. 3b), O1 exhibits a reorganization of its βA′ strand (Fig. 3c). This strand does not pair with βG. Instead, it H-bonds to the terminal portion of βB giving rise to a βA/βA′–βB–βE–βD β-sheet. O1 thus exhibits a topology somewhat reminiscent of the C1-set in which the β-sandwich is contributed by two 4-stranded (βA–βB–βE–βD and βG–βF–βC–βC′) β-sheets (Fig. 3a). The βA′ repositioning seen in the orthorhombic crystal form is also independently observed in the trigonal space group (*vide infra*), indicating that this is a genuine feature of the O1 Ig domain.

O1 flexibility

The availability of the M10:O1 structure in two alternative crystal forms allows for a comparative structural analysis. M10 domains in the trigonal (M10^T) and orthorhombic (M10^O) space groups are essentially identical. They display an rmsd of 0.57 Å for 95 aligned C$^\alpha$ atoms. Similarly, low rmsd values
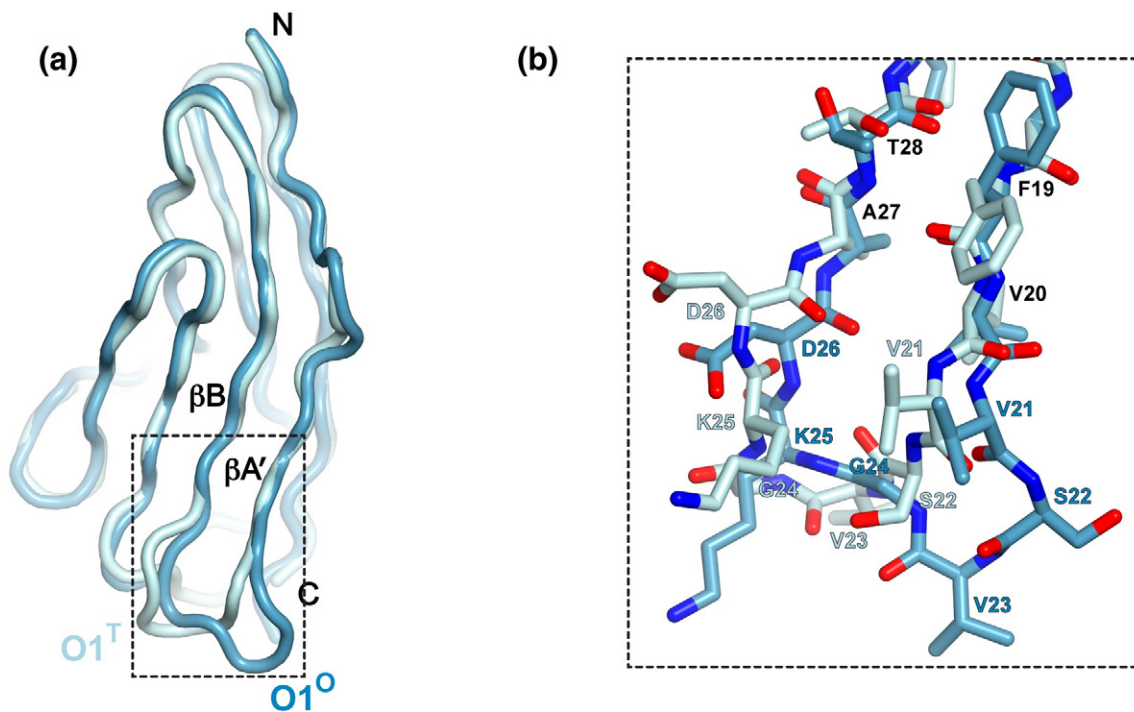
Fig. 4. The O1 βA′B loop displays alternative conformations in the crystal state. (a) Tube cartoon superposition of the O1 domains from the M10:O1 complexes solved in the trigonal (O1^T, light blue) and orthorhombic (O1^O, blue) space groups. The βA′B loop in the two structures (boxed area) is in a different conformation. (b) Close-up stick representation of the boxed area in panel a. Residues labeled in light and darker blue highlight the different structure of the βA′B loop in O1^T and O1^O, respectively.
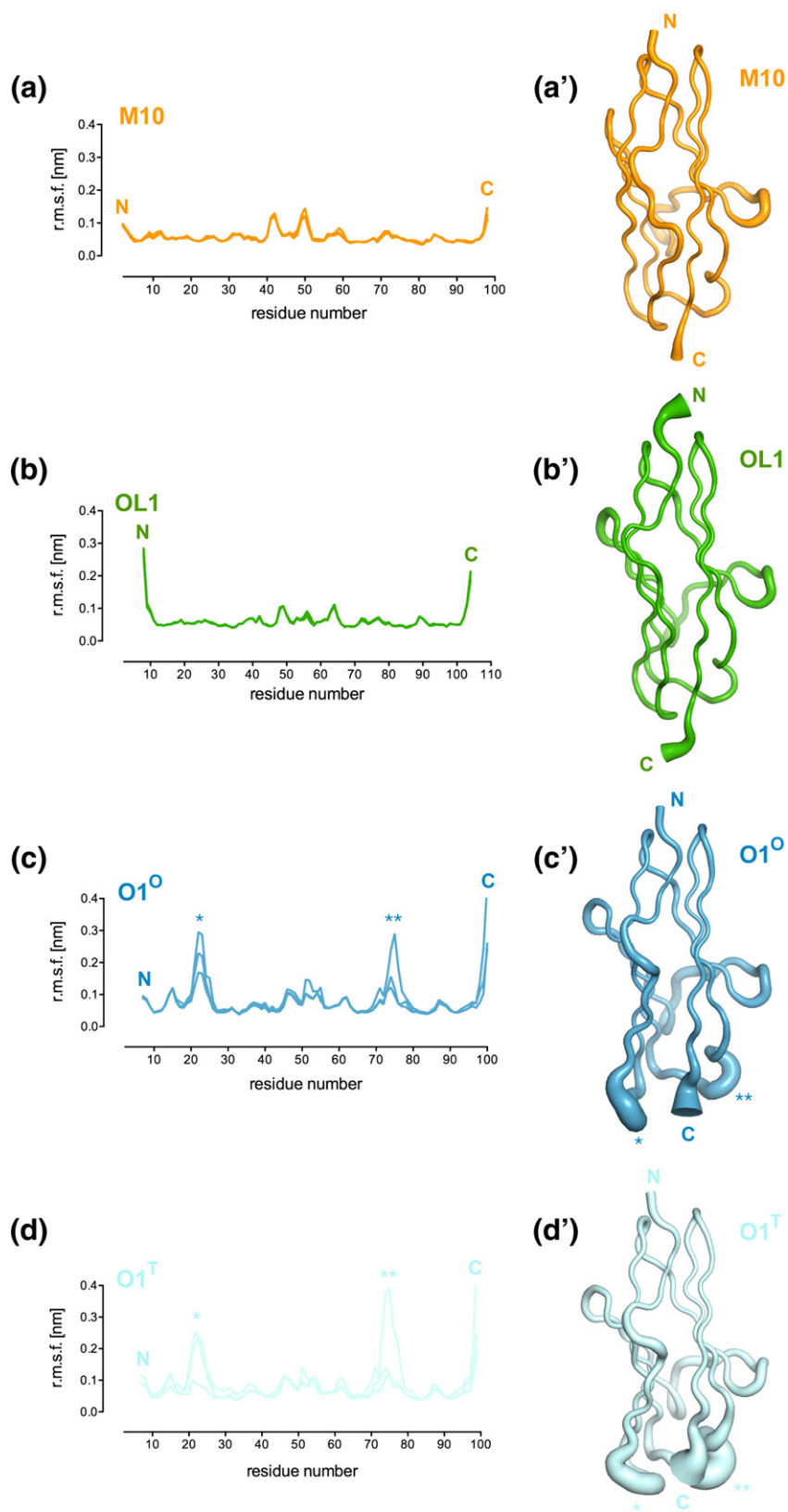
Fig. 5 (*legend on next page*)

are also obtained when the alignment is performed using the M10 domain solved in isolation [Protein Data Bank (PDB) code 2Y9R] or the M10 domain from M10:OL1 complexes solved in three alternative space groups. Thus, the conventional I-set M10 domain is a rigid scaffold exhibiting very limited structural variability. On the other hand, $O1^T$ and $O1^O$ display a core rmsd of 1.08 Å for 92 aligned C^α atoms. The region largely responsible for the higher deviation is the loop region connecting the βA′ and βB strands, which is in different conformations in the two space groups (Fig. 4). This is quantified, for example, by the intraloop distance between the C^α atoms of $O1^{S22}$ and $O1^{D26}$. This distance is 7.85 Å and 12.3 Å in $O1^T$ and $O1^O$, respectively. Furthermore, DSSP analysis [22] classifies the Ser8-Val20 region in $O1^T$ as a long βA strand, thus enhancing the similarity of this domain with the C1-set (Fig. 3b). A three-dimensional alignment against the PDB database [23] performed using the PDBeFold server [24] retrieved, however, I-set Ig domains as the most structurally similar to O1 with the Ig domain of human Aortic Preferentially Expressed Protein-1 [25] being the closest match (Q score = 0.79). Thus, O1 should be considered an I-set Ig domain exhibiting an unconventional βA′ arrangement.

To seek an independent validation of the apparent flexibility of the βA′–βB region in O1, we performed molecular dynamics (MD) simulations. Three independent replicas of 100-ns simulations were run for isolated conventional I-set domains (M10 and OL1) and O1. The time evolution of the root-mean-square deviation (rmsd) from the starting equilibrated structure is shown in Fig. S3. The root-mean-square fluctuation (rmsf) of the C^α coordinates from the average structures, a measure of the structural changes during the simulations, is given as residue-based plot and as cartoon-sausage representation in Fig. 5. While the conventional M10 and OL1 I-set domains are remarkably stable, the O1 domain exhibits flexibility particularly for the βA′–βB region (centred on residue 22), the βE–βF loop where the short α1 helix is located (residue 74) and the C-terminus. Thus, it appears that βA′ repositioning, which results in the loss of the cluster of βA′–βG hydrogen bonds typical of the conventional I-set, enhances local flexibility.

How frequent is the I-set βA′ repositioning observed in O1?

The deviant I-set topology observed for O1 in the M10:O1 complex led us to ask whether other known I-set Ig structures display a similar βA′ repositioning. We selected all proteins in the Pfam database [26] annotated to contain one or more I-set domains and we retrieved the corresponding structures from the PDB [23]. We then performed a comparative structural analysis (see Materials and Methods for details) to identify I-set domains exhibiting a relocation of the βA′ hydrogen-bonding pattern from βG to βB indicative of the switch. The bioinformatics analysis revealed that this topological variation is uncommon. Of a total of 173 unique I-set Ig domains present in the PDB (filtering at 95% sequence identity), only 8 (including O1, 4.6%) exhibit a relocation of their βA′ to the βA(/βA′)–βB–βE–βD sheet (Fig. 6). For convenience, we refer to these variants as the I*-set. Four I*-set domains are found in the muscle protein myomesin. This protein cross-links myosin filaments and has been suggested to provide elasticity and to help maintain the overall structural organization of the muscle fibers [27]. Its C-terminal My9–My12 region (myomesin Ig domains 9–12) is composed of an array of virtually identical I*-set structural modules followed by helical connectors [27]. Functionally, the I*-set topology allows the positioning of the C-terminal helices to generate a superhelical arrangement while providing intramolecular stabilization. Three structurally similar I*-set domains are also found in the Trk family of tyrosine kinases receptors that bind ligand neutrophins, growth factors critical to the functioning of the nervous system. TrkA/B/C domain 5 (d5) structures both in the free state [28] and in the neutrophins-bound form [29,30] feature their βA′ bound to βB. Repositioning of the βA′ strand helps in stabilizing the d5–neutrophins complex. Our analysis also revealed that the fifth Ig domain of human Kirrel3 (kin of irregular chiasm-like protein 3) solved by NMR exhibits a very mobile βA′ strand exhibiting limited interactions with either βG or βB. Thus, Kirrel3-Ig5 can be considered somewhat in between the I-set and I*-set. This domain is currently functionally uncharacterized. Overall, our analysis suggests that βA′ switch is evolutionarily rare. When present, it typically mediates specific inter- or intramolecular protein–protein interactions.

Fig. 5. MD simulations reveal an enhanced flexibility of O1 compared to conventional I-set domains. (a–d) rmsf from the average structure for M10 (a), OL1 (b), $O1^O$ (c), and $O1^T$ (d). Three replica simulations of 100-ns were run for each domain. The time evolution of the rmsd from the starting equilibrated structure is shown in Fig. S4. (a′–d′) Cartoon-sausage rmsf representation of M10 (a′), OL1 (b′), $O1^O$ (c′), and $O1^T$ (d′). The width of the tube is proportional to the degree of flexibility defined as rmsf from the average position of C^α atoms and calculated from the combination of the three replicas for each domain. While the conventional M10 and OL1 I-set domains are remarkably stable, the O1 domain exhibits flexibility for the βA′–βB region (*), the βE–βF loop where the short α1 helix is located (**), and the C-terminus (C).
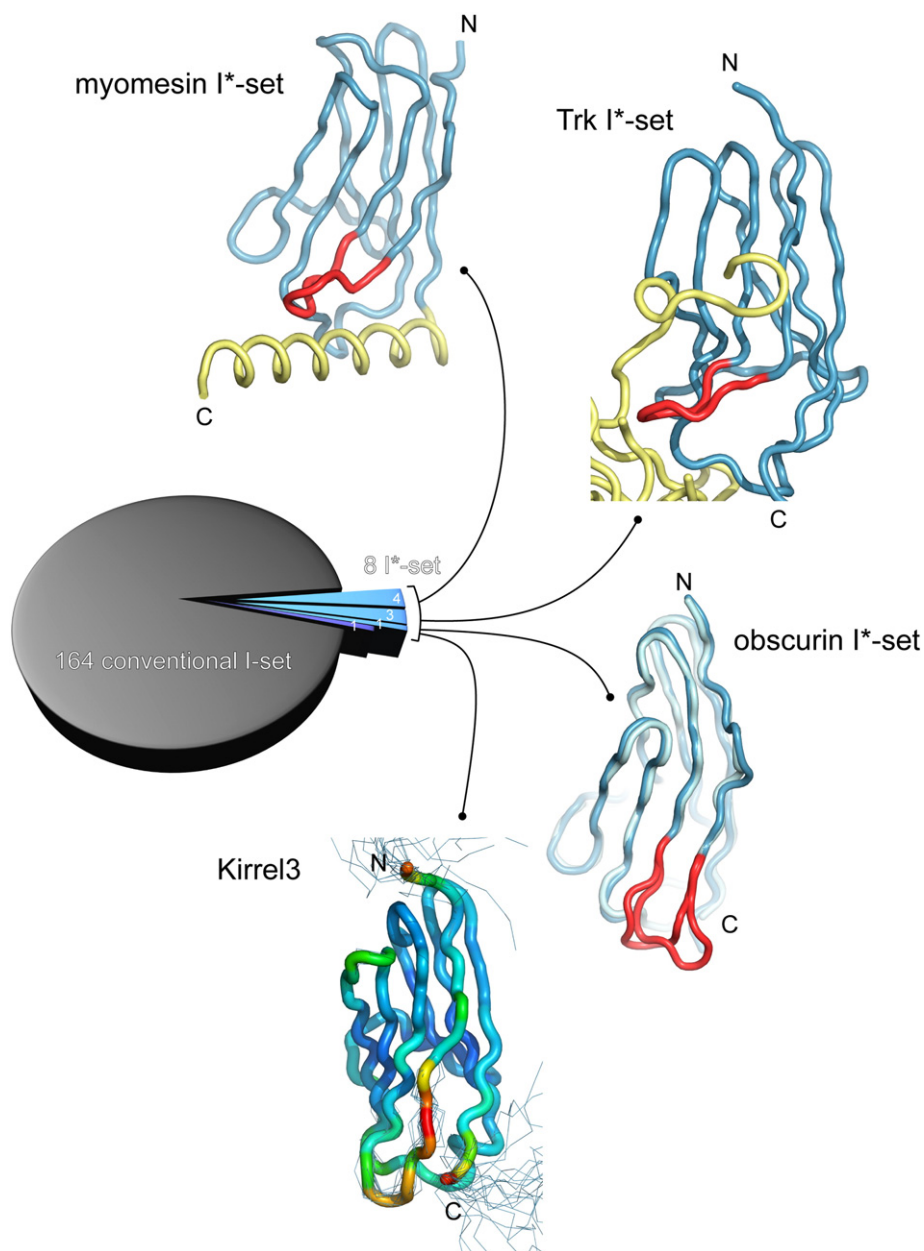
Fig. 6. The I*-set is a small subset of the I-set. Out of 173 structurally characterized unique I-set domains, 164 display the conventional I-set topology (gray in the pie chart, 94.8%) while 8 (blue, 4.6%) exhibit a relocation of their βA′ such that it is H-bonded to βB instead of βG. We defined this unconventional I-set as the I*-set. I*-set domains fall into three groups: myomesin I*-set—an array of four structurally identical I*-set domains (My9, My10, My11, and My12) are found in myomesin. My10 from PDB 2Y23 [27] is shown as an example. The Ig domain is shown in blue with its C-terminal helical extension in yellow. The βA′–βB region is highlighted in red. The βA′ strand makes room and provides intramolecular stabilization to the C-terminal helix; Trk I*-set—three I*-set domains are present in the Trk receptors (TrkA, TrkB, and TrkC). The TrkB-d5 Ig domain (blue) in complex with neurotrophin-4/5 (yellow) from PDB 1WWW [30] is given as an example. The relocated βA′ and the βA′–βB loop (red) strand stabilize the intermolecular interaction with the ligand; obscurin I*-set—the O1 domain of obscurin was identified in this work as an I*-set. O1^T and O1^O (light and darker blue, respectively) highlight alternative conformations of the βA′–βB loop (red); Kirrel3—the functionally uncharacterized fifth Ig domain of Kirrel3 solved by NMR (PDB 2CRY) exhibits a βA′ strand with limited interactions with either βG or βB. Thus, it is somewhat in between the I-set and the I*-set. The βA′ strand and βA′–βB loop region display together with the domain termini the highest structural variability as shown by the cartoon tube representation. The average structure is shown as rainbow gradient ranging from blue (lowest variability) to red (highest variability). C$^\alpha$ traces of the 20 individual NMR models are also shown.
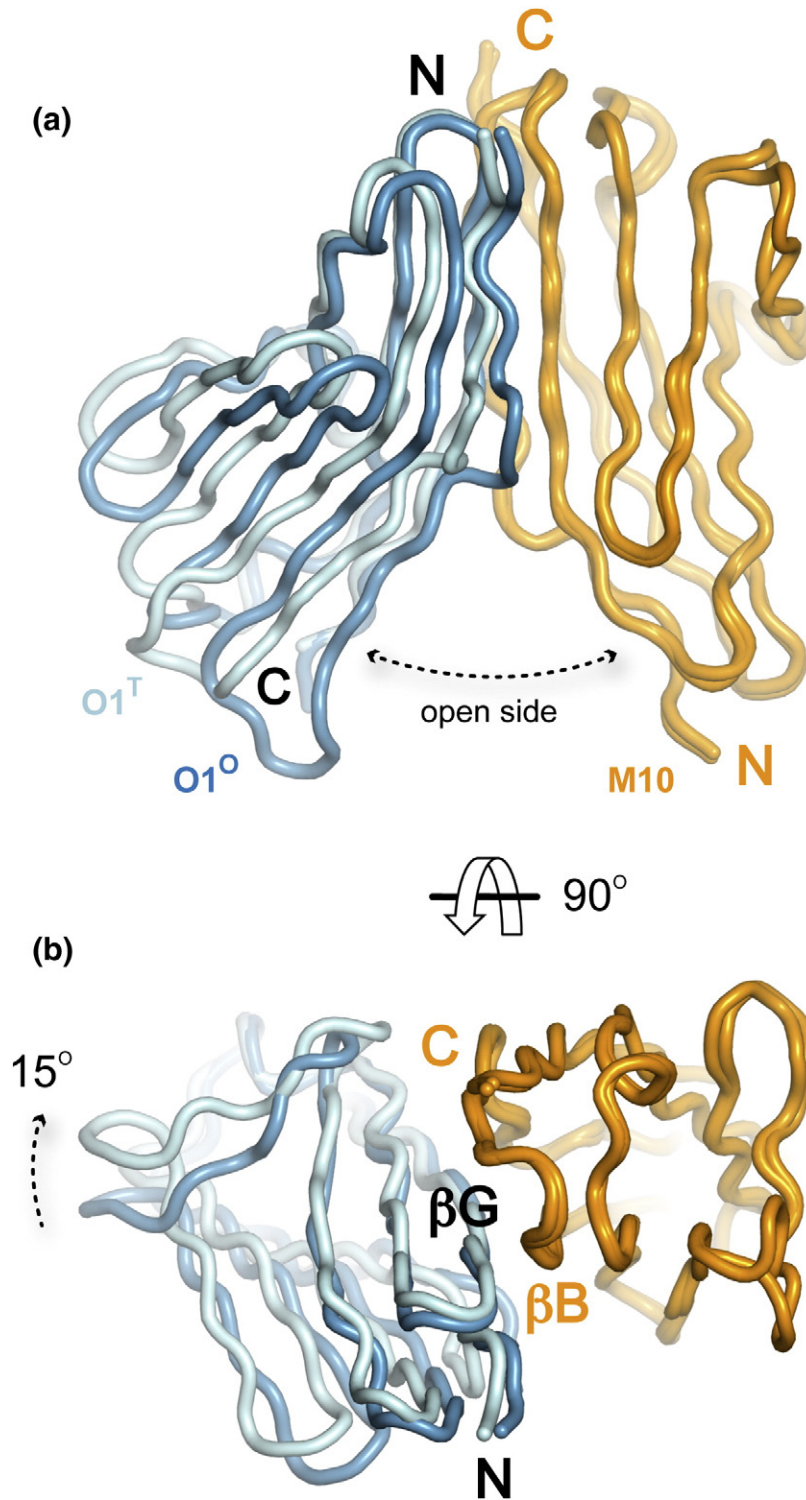
Fig. 7. M10:O1 hinge rotation. (a and b) Orthogonal views of the M10:O1 complexes in the trigonal and orthorhombic space groups superimposed using their M10 domains. M10 is shown in orange. O1 domains are color coded as in Fig. 4. The O1 domains show a hinge rotation of approximately 15° about the βG strand. The latter is largely responsible for establishing the molecular interface with M10 βB by β-strand augmentation. The chevron shape of the complex coupled with βA′B loop plasticity results in a variable geometry for the open side as a result of the hinge rotation.

M10:O1 hinge movement

The M10 domain is a scaffold exhibiting very limited structural variability. The M10:O1 complexes can thus be superposed with respect to their rigid M10 common frame to highlight overall O1 displacements. Following M10^T superposition to M10^O, O1^T and O1^O exhibit an rmsd of 3.05 Å for their equivalent C$^\alpha$ atoms. This large displacement results from a rotation about the βG strand "axis" of

more than 15° (Fig. 7). Such a "hinge" rotation leaves the M10:O1 molecular interface, which is largely directed by the H-bonding between O1 βG and M10 βB, unaffected, while altering the width of the open side of the complex. For example, the C$^\alpha$ atoms of Gly24, a very conserved βA′B loop residue in the I-set [21], are displaced by 9.2 Å in the different crystal forms (Fig. S4). The main reason for this hinge rotation appears to be alternative crystal packing. In the trigonal form, all 18 M10:O1
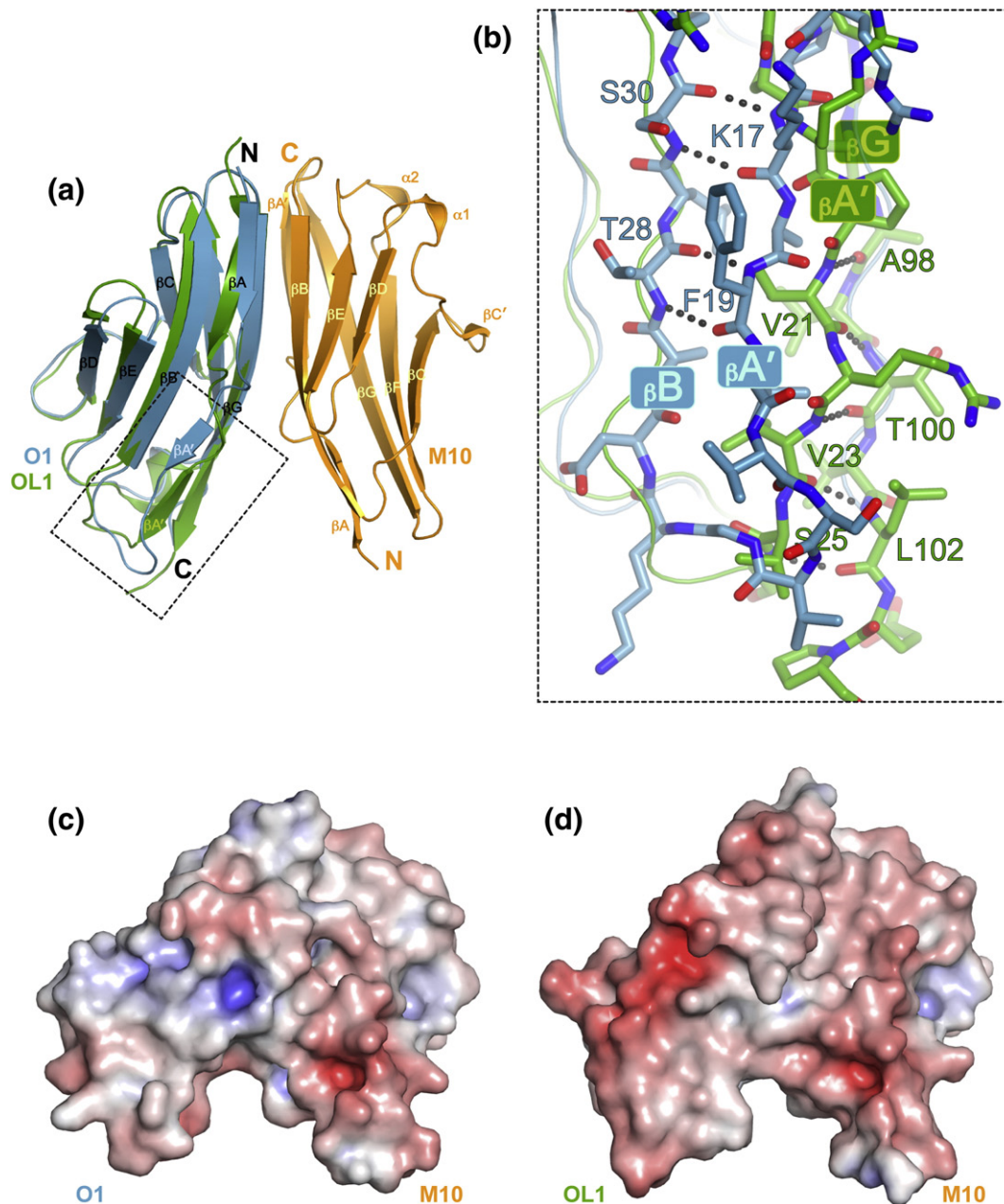
Fig. 8. M10:O1 and M10:OL1. (a) Cartoon superposition of the M10:O1 and M1O:OL1 complexes. As in previous figures, M10 and O1 are shown in orange and blue, respectively. OL1 is in green. (b) Stick representation of the βA′B region of O1 and OL1 highlighting their orthogonal βA′ strands. (c and d) Electrostatic surface representations of M10:O1 (c) and M10:OL1 (d).

complexes pack in a similar way with their "chevrons" wedged inside each other generating continuous helices in the crystal (Fig. S5). On the other hand, the packing arrangement in the orthorhombic form leaves the open side of the chevron much more solvent accessible (Fig. S6). From a functional perspective, this observation indicates that weak alternative crystal packing forces are able to capture a degree of M10:O1 structural adaptability achieved by coupling O1 βA′B loop plasticity to a hinge rotation resulting in rather large variations for the open side of the chevron-shaped complex.

Comparison between M10:O1 and M10:OL1

M10:O1 and M10:OL1 are very similar overall (Fig. 8a). This was predicted on the basis of their conserved interface residues (Fig. 2d), similar binding affinities in the low micromolar range (Table 2), and a virtually identical behavior in single-molecule force-extension experiments with both complexes yielding at low forces around 30 pN [17]. Topological differences between O1 and OL1 have nevertheless implications for the fine structural properties of the complexes. Like M10, OL1 folds in a conventional I-set with its βA′ strand hydrogen bonded to βG. This results in the βA′ strands of O1 and OL1 being roughly orthogonal with respect to each other (Fig. 8a and b). As a consequence, while alternate OL1 βA′ side chain abut onto the open side of the chevron narrowing it, the equivalent side chains in O1 βA′ point away from the intermolecular space. Conversely, main-chain atoms of the O1 Pro16-Val21 stretch face the open side of the complex. Amino acid differences between O1 and OL1 also contribute to alternative electrostatic potentials in the two complexes (Fig. 8c and d).

Although residues at the molecular interface are highly conserved, a striking difference is the replacement of OL1 F17 with an arginine residue (R15)

in O1 (Fig. 2d). These residues map at the top of the cavity defined by the chevron-shaped architecture and are totally conserved within the vertebrate Obsl1 and obscurin families, respectively, effectively representing a signature of their Ig domains. Previous isothermal titration calorimetry (ITC) measurements (Table 2) and pull-down experiments have shown that replacement of residue OL1 F17 with an arginine residue (OL1^{F17R}) diminishes the affinity of this domain for M10 compared to wild-type OL1 [17]. Conversely, the R15F variation in O1 (O1^{R15F}) results in a higher affinity for M10 compared to both wild-type O1 and OL1. However, the OL1^{F17R} mutation mimics O1 only partially as the X-ray structure of the M10:OL1^{F17R} complex shows that OL1^{F17R} retains the I-set topology. This suggests that the I*-set is unlikely the product of a single amino acid substitution and that it requires the coevolution of residues on adjacent strands permissive of such topological change.

The X-ray structure of the complexes suggests that the interaction between M10 and its O1/OL1 binding partners should be largely insensitive to the alternative locations of βA′ strand as the latter is not directly involved in the establishment of the molecular interface. To test this, we generated M10^{A25K}, M10^{A25E}, M10^{D60R}, and M10^{L61R} variants and tested their binding to O1 and OL1 by ITC. Residues A25, D60, and L61 are on the M10 surface and in the proximity of O1/OL1. The M10 variants exhibited 1.6- to 4-fold lower affinities compared to wtM10 (Table 2). However, none of the mutants tested displayed a significant differential affinity for its O1 or OL1 binding partner. This further supports the notion that the binary M10:O1 and M10:OL1 interactions are essentially insensitive to the topological difference between O1 and OL1.

Table 2. Isothermal titration calorimetry

Interaction	*N*	K_d (µM)	ΔH (kcal/mol)	$T\Delta S$ (kcal/mol)	ΔG (kcal/mol)
M10–O1	*1.050 ± 0.005*	*2.70 ± 0.15*	*11.16 ± 0.68*	*18.6*	*−7.4*
	0.82 ± 0.03	*5.08 ± 1.21*	*6.31 ± 0.42*	*13.4*	*−7.1*
M10–OL1	*1.040 ± 0.008*	*0.79 ± 0.09*	*3.87 ± 0.34*	*12.0*	*−8.1*
	1.07 ± 0.01	*1.34 ± 0.16*	*3.70 ± 0.05*	*11.6*	*−7.9*
M10–O1^{R15F}	*1.040 ± 0.003*	*0.41 ± 0.02*	*5.64 ± 0.18*	*8.6*	*−7.9*
M10–OL1^{F17R}	*0.990 ± 0.014*	*1.28 ± 0.21*	*0.66 ± 0.11*	*14.2*	*−8.6*
M10–O1^{A94Y}	—	No binding	—	—	—
M10–OL1^{A96Y}	—	No binding	—	—	—
M10^{A25K}–O1	1.12 ± 0.04	11.01 ± 2.97	0.48 ± 0.03	7.1	−6.6
M10^{A25K}–OL1	0.83 ± 0.04	2.16 ± 0.41	4.10 ± 0.30	10.4	−6.3
M10^{A25E}–O1	0.87 ± 0.04	16.86 ± 3.47	3.98 ± 0.25	10.4	−6.4
M10^{A27E}–OL1	0.91 ± 0.03	5.43 ± 0.98	3.56 ± 0.15	10.6	−7.1
M10^{D60R}–O1	0.89 ± 0.04	15.20 ± 3.28	2.15 ± 0.14	8.6	−6.5
M10^{D60R}–OL1	1.03 ± 0.01	4.39 ± 0.52	2.83 ± 0.05	10.0	−7.2
M10^{L61R}–O1	0.89 ± 0.05	19.19 ± 4.75	1.64 ± 0.13	8.0	−6.3
M10^{L61R}–OL1	1.19 ± 0.04	4.48 ± 1.28	0.25 ± 0.01	7.4	−7.2

Data in italics are from Ref. [17].

Cellular competition assay in neonatal rat cardiomyocytes

Analysis of the M10:O1 and M10:OL1 structures highlighted a limited number of residues whose replacement would prevent complex formation. One such position is occupied by A94 and A96 in O1 and OL1, respectively (Fig. 9a). The methyl group of the side chain faces M10^{P11} and a large residue at this position is not compatible with a stable complex. ITC measurements confirmed that when O1^{A94} and OL1^{A96} are replaced by a tyrosine residue, binding is totally abolished (Table 2, Fig. 9b, and Fig. S7). To validate the M10:O(L)1 interaction in the context of the sarcomere, we tested O1^{A94Y} and OL1^{A96Y} variants in a cellular competition assay and
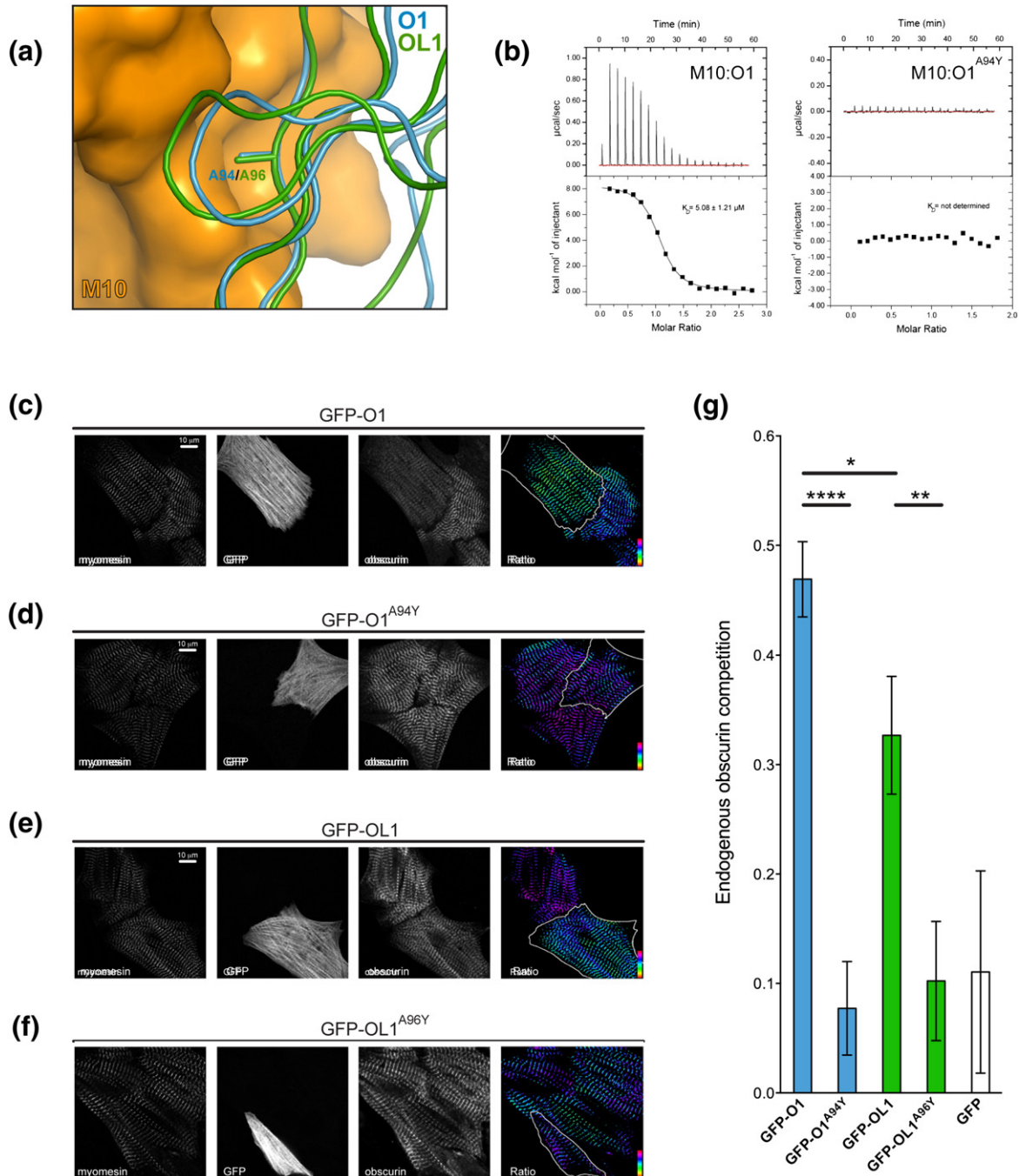

Fig. 9 (*legend on next page*)

compared their behavior to the wild-type domains. When overexpressed in neonatal rat cardiomyocytes (NRCs), GFP-O1 or GFP-OL1 targets the sarcomeric M-band, in addition to other diffuse subcellular localizations, displacing endogenous obscurin (Fig. 9c and e) [2]. This is fully consistent with a mutually exclusive binding of O1 and OL1 to M10. Overexpression of GFP-O1^{A94Y} and GFP-OL1-^{A96Y} in NRCs leads to a significant reduction of displaced endogenous obscurin (Fig. 9d and f). This is quantified in Fig. 9g. Both GFP-O1^{A94Y}/GFP-O1^{A96Y} variants fail to displace obscurin above the level of green fluorescent protein (GFP) control in agreement with structural and biophysical (ITC) data. Importantly, our quantitative analysis also shows that GFP-O1 competes endogenous obscurin better than GFP-OL1 (p value = 0.0324) in spite of the slightly higher affinity of OL1 for M10 compared to O1 (Table 2). One possible explanation for this observation is that in the NRCs, in addition to titin (M10), one or more additional binding partners are associated with the obscurin domain O1 resulting in a complex of higher order than the binary M10:O1 interaction. In this scenario, it is reasonable that GFP-O1 is able to compete endogenous obscurin better than GFP-OL1 as the latter domain can provide an optimal interface for M10 but presumably not for other binding partners associated with the M10:O1 complex. It is tempting to speculate that architectural differences between M10:O1 and M10:OL1 underpin their potential binding specificity at the M-band.

Concluding remarks

The M-band C-terminus of titin binds the N-terminus of obscurin at the myofibril periphery and the N-terminus of Obsl1 at the myofibrillar inner core. These interactions are mutually exclusive and are directed by the M10 Ig domain of titin engaging either the O1 Ig domain of obscurin or the OL1 Ig domain of Obsl1. Currently, titin's M10, a frequent target

of disease-linked mutations, is the only known muscle Ig domain able to interact with two alternative ligands. The M10:O1 and M10:OL1 share an identical architecture with the two Ig domains arranged head to tail, giving rise to a chevron-shaped complex stabilized by parallel intermolecular β-sheet augmentation. Unexpectedly, the O1 domain, differently from both M10 and OL1, displays an evolutionarily rare I-set variant topology, whereby the βA′ strand hydrogen-bonds to the terminal portion of βB instead of exhibiting the typical switch to the βG–βF–βC–βC′ β-sheet. We identified this I-set variant as the I*-set. It is tempting to speculate that such topological alteration, which does not affect the direct interaction with M10, might regulate the binding of alternative partners. A few observations suggest that this hypothesis warrants further investigations. The I-set topology is generally very well conserved among cytoskeletal proteins. We noticed that the few I*-set domains characterized structurally and biochemically typically employ their deviant βA′ strands to direct either intermolecular (Trk) or intramolecular (myomesin) interactions. Additionally, single-molecule force-extension experiments show that both M10:O1 and M10:OL1 complexes yield at forces around 30 pN [17]. This is indicates a very low mechanical stability when compared, for example, to the Z-band telethonin–titin complex, which requires around 800 pN to dissociate [31]. Although the muscle M-band is more compliant than the Z-disk [1], it is nevertheless surprising that binary M10:O1 and M10:OL1 complexes possess such a low mechanical stability. This could suggest that additional factors are required to increase their mechanical strength. Our assays in NRCs suggest that additional elements of specificity might be involved, possibly by ternary interactions of the M10:O1 complex, as the competition of OL1 seems lower in the cellular context. The O1 and OL1 modules appear perfectly poised as discriminatory structural elements potentially involved in the binding of additional specific partners.

Fig. 9. Biophysical and cellular validation in NRCs. (a) Close-up of the M10:O1/OL1 interface. M10 is shown as surface representation in orange. O1 and OL1 are shown as tubes in blue and green, respectively. The side chains of O1^{A94} and OL1^{A96} are shown as sticks. A bulky residue at the O1^{A94}/OL1^{A96} position is incompatible with complex formation. (b) ITC measurements confirm that the O1^{A94Y} variant is unable to bind to M10 (right-hand panel). Data for the M10:O1 interaction is shown in the left-hand panel as reference. The OL1^{A96Y} variant behaves in an identical manner as O1^{A94Y} (Table 2 and Fig. S6). (c) Example of the competitive effect of overexpressed GFP-fused O1 (GFP-O1) on endogenous obscurin in NRCs. The separate channels for endogenous myomesin, GFP, endogenous obscurin, and the ratiometric image with overlaid GFP mask for the outline of the transfected cell are shown. The false-color scale range indicator shows an increased obscurin/myomesin ratio. (d) Similar to panel c for overexpressed GFP-fused O1^{A94Y} (GFP-O1^{A94Y}). (e) Similar to panel c for overexpressed GFP-fused OL1 (GFP-OL1). (f) Similar to panel c for overexpressed GFP-fused OL1^{A96Y} (GFP-OL1^{A96Y}). (g) Quantification of endogenous obscurin displaced in NRCs expressing GFP-fused O1 ($n = 21$), OL1 ($n = 21$), O1^{A94Y} ($n = 21$), and OL1^{A96Y} ($n = 21$). GFP alone was also used as control ($n = 6$). Total obscurin displacement would be represented by a value of 1.0 on the y-axis whereas 0.0 indicates absence of competition. Both O1 and OL1 are able to compete endogenous obscurin. On the other hand, neither variant shows the ability to compete above GFP control levels in agreement with structural and biophysical (ITC) data. A two-tailed t test indicates that differences between O1 and O1^{A94Y} ($p < 0.0001$), between OL1 and OL1^{A96Y} ($p = 0.0055$), and between O1 and OL1 ($p = 0.0324$) are statistically significant (****$p \leq 0.0001$, ***$p \leq 0.001$, **$p \leq 0.01$, *$p \leq 0.05$). Error bars are SEM values.

Materials and Methods

Cloning and site-directed mutagenesis

DNA encoding for the last Ig domain of human titin (residues 34352–34350, henceforth M10 1–99), the first Ig domain of human obscurin (O1, residues 1–109), and the first Ig domain of human Obsl1 (OL1, residues 1–106) were amplified by PCR with custom oligonucleotides primers between the XhoI and BamHI restrictions sites of a in-house modified pET9 vector. Downstream the His$_6$-tag, this vector encodes for a tobacco etch virus protease recognition. Site-directed mutagenesis was performed using the Quik-Change kit. All constructs were verified by sequencing.

Protein expression and purification

All domains were expressed as N-terminal His$_6$-tagged fusion proteins in Rosetta 2(DE3) cells (Novagen). Transformed cells were grown in Luria–Bertani medium supplemented with 100 µg/ml ampicillin and 34 µg/ml chloramphenicol at 37 °C until OD$_{600}$ reached approximately 0.5. After decreasing the temperature to 18 °C, overnight protein expression was induced with 0.15 mM IPTG. Cells were harvested by centrifugation at 5000*g* for 15 min at 4 °C and resuspended in phosphate-buffered saline (PBS) lysis buffer in which NaCl concentration was increased to 250 mM. The cell suspension was supplemented with 2.4 U/ml of benzonase (Novagen), 0.25 mg/ml chicken egg white lysozyme (Novagen), and Complete EDTA-free protease inhibitor cocktail (Roche). Cell lysis was accomplished by two freeze-and-thaw cycles. Insoluble material was sedimented by centrifugation at 16,500*g* for 1 h at 4 °C and the supernatant was filtered using 0.22 µm prior to loading on a His-trap HP column (GE Healthcare) preequilibrated with the lysis buffer supplemented with 10 mM imidazole. His$_6$-tagged proteins were eluted with an imidazole linear gradient. Fractions containing the target His-tagged domains were collected and dialyzed overnight against PBS buffer. During dialysis, the purification tag was cleaved using tobacco etch virus protease. All cleavage products bear a GSS amino acid triplet at the N-terminus resulting from the cloning strategy. Uncleaved material was removed from the mixture sample loading the dialyzed protein solution on a His-trap HP column (GE Healthcare). Untagged material was collected, concentrated, and further purified by SEC on a 16/60 HiLoad Superdex 75 column (GE Healthcare) equilibrated with 20 mM Hepes, pH 7.5, 50 mM NaCl, and 1 mM DTT. M10, O1, OL1, and all variants (M10^{A25K}, M10^{A25E}, M10^{D60R}, M10^{L61R}, O1^{A94Y}, and OL1^{A96Y}) eluted from SEC as monomers. The M10:O1 complex used for crystallization was obtained mixing the individual components with a 1:1 molar ratio and allowing incubation on ice for 30 min. The complex was further purified by SEC as described above.

Crystal preparation

Crystallization trials were initially performed using M10:O1(1–109) and M10:O1(7–109) complexes by the vapor diffusion setup at 18 °C using a 1:1 protein:precipitant ratio in 400-nl sitting drops dispensed with the aid of Mosquito crystallization robot (TTP LabTech). These constructs failed to yield crystals of good quality. Over time, we observed proteolytic degradation of O1(7–109) leading to a marginally smaller fragment. This observation was further supported by limited proteolysis experiments. Elastase and proteinase K digestion led to a O1(7–109) truncation product virtually identical with that of the aged sample (Fig. S1). This led us to engineer O1 domains with marginally shorter C-termini. The crystallization of M10:O1(7–99) was pursued by both vapor diffusion and batch techniques. Batch crystallization screening performed at the Hauptman–Woodward Medical Research Institute (Buffalo, NY) produced initial hits that were judged more promising than those obtained by vapor diffusion methods. Crystallization conditions were further refined in-house using the batch setup. Crystals of M10:O1(7–99) belonging to space group *P*3$_2$21 were obtained using 0.1 M trisodium citrate, pH 3.6, and 3.0 M sodium chloride as precipitant. Crystals of M10:O1(7–103) belonging to space group *P*2$_1$2$_1$2$_1$ were obtained by the hanging drop method using 0.1 M Tris–HCl, pH 8.5, 0.2 M sodium acetate, and 30% polyethylene glycol 4000 as precipitant. Cryoprotection was performed in reservoir supplemented with 20% (v/v) ethylene glycol.

Data collection, structure solution, and crystallographic refinement

M10$^{1–99}$:O1$^{7–103}$ crystallizes in the orthorhombic space group *P*2$_1$2$_1$2$_1$ with a single heterodimer in the a.u. These crystals diffract to 1.95 Å resolution using synchrotron radiation (Table 1). M10$^{1–99}$:O1$^{7–99}$ crystals display a rod-shaped morphology with typical cross-dimensions of about 30 Å. They diffract X-rays rather poorly using synchrotron radiation and are radiation damage sensitive. An initial complete data set was collected at the I04 beamline (Diamond Light Source) at the 3.5-Å resolution. Matthews coefficient analysis in most probable 321 point group symmetry suggested a high number of molecules in the a.u. In consideration of the low diffracting power of these crystals, we believed the number of M10:O1 complexes in the a.u. to be between 13 (70% solvent content) and 22 (50% solvent content). A strong (0.000, 0.000, 0.424) peak in the native Patterson map corresponding to approximately 40% of the origin peak indicated the presence of translational NCS along the screw 3-fold axis. A molecular replacement search using the program *MOLREP* [32] and a template derived from the M10:OL1 complex identified 14 copies of the complex. However, voids in the packing arrangement suggested the presence of additional complexes. Later, a second data set was measured at the 3.3-Å resolution (Table 1) employing a wedged helical collection strategy at the microfocus I24 beamline (Diamond Light Source) and used for further crystallographic refinement. The high *R*$_{merge}$ statistics for this data set (21.5% overall, Table 1) is most likely related to its low $\langle I/\sigma(I) \rangle$ value as seen in other similar PDB depositions (e.g., 4PBA [33]). Improved electron density maps allowed manual positioning of four additional heterodimers. Overall, the complete model in the trigonal space group comprises 18 M10:O1 complexes corresponding to a 59% solvent content. Dramatic differences in crystal quality between M10$^{1–99}$:O1$^{7–103}$ and M10$^{1–99}$:O1$^{7–99}$ highlight the critical importance of subtle variations in construct design. Refinement of the complex in both space groups was carried out with

REFMAC5 [34] and BUSTER [35] using NCS restraints for the low-resolution data set. Data collection and refinement statistics are shown in Table 1.

Isothermal titration calorimetry

Samples for ITC measurements were extensively dialyzed in ITC buffer [20 mM Tris–HCl, pH 7.5, 50 mM NaCl, and 1 mM tris(2-carboxyethyl)phosphine–HCl]. ITC experiments were conducted on a MicroCal ITC (MicroCal Inc.) instrument at a temperature of 20 °C. Data were corrected for heats of dilution of the protein solution. Binding constants and other thermodynamic parameters were calculated by fitting the integrated titration data assuming a single set of binding sites using the Origin software package (OriginLab, Northampton, MA).

Bioinformatics analysis

A list of the known protein structures containing an I-set domain was derived from the Pfam database [26] entry PF07679. For each structure, the region encompassing the I-set domain was extracted from the corresponding PDB file and aligned with the O1 structure using TM-align [36]. The H-bonding pattern of the βA′ strand with the adjacent strands was detected using DSSP [22]. I-set Ig domains were classified as "conventional" if the βA′ was H-bonded to βG. They were classified as "I*" if βA′ was H-bonded to βB.

MD simulations

MD simulations of M10, OL1, and the two crystallographic forms of O1 were performed with GROMACS 4.6.2 [37] using the ff-amber99sb-ILDN [38] porting of the AMBER parm99 parameter set. The initial structures were solvated with a cubic box of TIP3P water molecules. Ionizable residues were modeled in their standard protonation state at pH 7.0. The systems were then neutralized adding the appropriate number of counterions. System equilibration and thermalization was performed as previously described [39]. Production simulations were performed in the NPT ensemble and periodic boundary conditions were imposed. All the bonds were frozen and a 2-fs time step was used. Electrostatic interactions were calculated with the particle mesh Ewald method with a 14-Å cutoff for the direct space sums, a 1.2-Å fast Fourier transform grid spacing, and a four-order interpolation polynomial for the reciprocal space sums. For van der Waals interactions, a 14-Å cutoff was used. The neighbor list for noncovalent interactions was updated every five steps. Three replicas of 100-ns simulations were generated for each system.

Cellular competition assays in NRCs and ratiometric analysis

NRC isolation, culture, transfection, and staining were performed essentially as described previously [17]. Briefly, NRCs were transfected with GFP-tagged transiently expressing constructs (pEGFPC2-, Clontech) using Escort III (Sigma Aldrich). After 48 h culture to promote protein expression, cells were fixed with 4% paraformaldehyde/PBS, permeabilized with 0.1% Triton X-100/PBS, and then stained with the appropriate antibodies. The antibodies used for the current work were as follows: MyB4, a mouse monoclonal antibody to the myomesin domain My12 [40]; and Ob5859, a rabbit polyclonal antibody to two consecutive Ig domains in obscurin, Ob58 and Ob59 [41,42]. All fluorescent-conjugated secondary antibodies were purchased from Jackson ImmunoResearch (USA). All images for ratiometry analysis were collected by a Zeiss LSM510 confocal microscope basically as described previously [2]. To see the competitive effect of overexpressed GFP-O1 or GFP-OL1 and their variants on endogenous obscurin, we imported 16-bit-per-channel RGB files into Mathematica 10 and translated them to ensure correct alignment of the myomesin and obscurin channels. Background subtraction was performed on these channels by subtracting a 50-pixel radius Gaussian filtered version of that channel. The arctangent of the obscurin and myomesin intensities was then calculated on a pixel-by-pixel basis to give a ratio image of obscurin to myomesin that was linearly scaled between 0 and 1. A value of 0 corresponded to no obscurin in the presence of myomesin, while a value of 1 corresponded to obscurin in the absence of myomesin. A value of 0.5 corresponded to equal intensities in both channels. The GFP channel was binarized to create a segmented image corresponding to GFP-positive and GFP-negative regions. The ratio image was multiplied by this mask and separately with an inverted version of this mask to give two ratio images that corresponded to the GFP-positive and GFP-negative regions of the image as two separate images. A histogram for each image was then determined and normalized to a total of 1 for each histogram. Plotting these against each other thus allowed comparison in shifts in ratio. A left shift (towards zero) indicated a reduction of obscurin in the GFP-positive ratio image. The difference between the two curves in this direction was calculated and the data presented represent one minus the total integrated difference between these two; thus, a value of 1 here represented total competition of the GFP fusion for endogenous obscurin, while a value of 0 represented no competition.

Accession numbers

Coordinates and structure factors have been deposited in the PDB with accession numbers 4UOW and 4C4K.

Appendix A. Supplementary data

Supplementary data to this article can be found online at http://dx.doi.org/10.1016/j.jmb.2014.11.019.

References

[1] Gautel M. The sarcomeric cytoskeleton: who picks up the strain? Curr Opin Cell Biol 2011;23:39–46.

[2] Fukuzawa A, Lange S, Holt M, Vihola A, Carmignac V, Ferreiro A, et al. Interactions with titin and myomesin target obscurin and obscurin-like 1 to the M-band: implications for hereditary myopathies. J Cell Sci 2008;121:1841–51.

[3] Pollazzon M, Suominen T, Penttila S, Malandrini A, Carluccio MA, Mondelli M, et al. The first Italian family with tibial muscular dystrophy caused by a novel titin mutation. J Neurol 2009;257:575–9.

[4] Udd B. Third filament diseases. Adv Exp Med Biol 2008;642:99–115.

[5] Bagnato P, Barone V, Giacomello E, Rossi D, Sorrentino V. Binding of an ankyrin-1 isoform to obscurin suggests a molecular link between the sarcoplasmic reticulum and myofibrils in striated muscles. J Cell Biol 2003;160:245–53.

[6] Kontrogianni-Konstantopoulos A, Jones EM, Van Rossum DB, Bloch RJ. Obscurin is a ligand for small ankyrin 1 in skeletal muscle. Mol Biol Cell 2003;14:1138–48.

[7] Lange S, Ouyang K, Meyer G, Cui L, Cheng H, Lieber RL, et al. Obscurin determines the architecture of the longitudinal sarcoplasmic reticulum. J Cell Sci 2009;122:2640–50.

[8] Lange S, Perera S, Teh P, Chen J. Obscurin and KCTD6 regulate cullin-dependent small ankyrin-1 (sAnk1.5) protein turnover. Mol Biol Cell 2012;23:2490–504.

[9] Raeker MO, Russell MW. Obscurin depletion impairs organization of skeletal muscle in developing zebrafish embryos. J Biomed Biotechnol 2011;2011:479135.

[10] Kontrogianni-Konstantopoulos A, Ackermann MA, Bowman AL, Yap SV, Bloch RJ. Muscle giants: molecular scaffolds in sarcomerogenesis. Physiol Rev 2009;89:1217–67.

[11] Arimura T, Matsumoto Y, Okazaki O, Hayashi T, Takahashi M, Inagaki N, et al. Structural analysis of obscurin gene in hypertrophic cardiomyopathy. Biochem Biophys Res Commun 2007;362:281–7.

[12] Kim JH, Park BL, Pasaje CF, Kim Y, Bae JS, Park JS, et al. Contribution of the OBSCN Nonsynonymous Variants to Aspirin Exacerbated Respiratory Disease Susceptibility in Korean Population. DNA Cell Biol 2012;31:1001–9.

[13] Huber C, Fradin M, Edouard T, Le Merrer M, Alanay Y, Da Silva DB, et al. OBSL1 mutations in 3-M syndrome are associated with a modulation of IGFBP2 and IGFBP5 expression levels. Hum Mutat 2009;31:20–6.

[14] Hanson D, Murray PG, Sud A, Temtamy SA, Aglan M, Superti-Furga A, et al. The primordial growth disorder 3-M syndrome connects ubiquitination to the cytoskeletal adaptor OBSL1. Am J Hum Genet 2009;84:801–6.

[15] Huber C, Dias-Santagata D, Glaser A, O'Sullivan J, Brauner R, Wu K, et al. Identification of mutations in CUL7 in 3-M syndrome. Nat Genet 2005;37:1119–24.

[16] Litterman N, Ikeuchi Y, Gallardo G, O'Connell BC, Sowa ME, Gygi SP, et al. An OBSL1-Cul7Fbxw8 ubiquitin ligase signaling mechanism regulates Golgi morphology and dendrite patterning. PLoS Biol 2011;9:e1001060.

[17] Pernigo S, Fukuzawa A, Bertz M, Holt M, Rief M, Steiner RA, et al. Structural insight into M-band assembly and mechanics from the titin-obscurin-like-1 complex. Proc Natl Acad Sci U S A 2010;107:2908–13.

[18] Sauer F, Vahokoski J, Song YH, Wilmanns M. Molecular basis of the head-to-tail assembly of giant muscle proteins obscurin-like 1 and titin. EMBO Rep 2010;11:534–40.

[19] Arvanitis DA, Sanoudou D, Kolokathis F, Vafiadaki E, Papalouka V, Kontrogianni-Konstantopoulos A, et al. The Ser96Ala variant in histidine-rich calcium-binding protein is associated with life-threatening ventricular arrhythmias in idiopathic dilated cardiomyopathy. Eur Heart J 2008;29:2514–25.

[20] Otey CA, Dixon R, Stack C, Goicoechea SM. Cytoplasmic Ig-domain proteins: cytoskeletal regulators with a role in human disease. Cell Motil Cytoskeleton 2009;66:618–34.

[21] Harpaz Y, Chothia C. Many of the immunoglobulin superfamily domains in cell adhesion molecules and surface receptors belong to a new structural set which is close to that containing variable domains. J Mol Biol 1994;238:528–39.

[22] Kabsch W, Sander C. Dictionary of protein secondary structure: pattern recognition of hydrogen-bonded and geometrical features. Biopolymers 1983;22:2577–637.

[23] Berman HM, Battistuz T, Bhat TN, Bluhm WF, Bourne PE, Burkhardt K, et al. The Protein Data Bank. Acta Crystallogr D Biol Crystallogr 2002;58:899–907.

[24] Krissinel E, Henrick K. Secondary-structure matching (SSM), a new tool for fast protein structure alignment in three dimensions. Acta Crystallogr D Biol Crystallogr 2004;60:2256–68.

[25] Manjasetty BA, Niesen FH, Scheich C, Roske Y, Goetz F, Behlke J, et al. X-ray structure of engineered human Aortic Preferentially Expressed Protein-1 (APEG-1). BMC Struct Biol 2005;5:21.

[26] Punta M, Coggill PC, Eberhardt RY, Mistry J, Tate J, Boursnell C, et al. The Pfam protein families database. Nucleic Acids Res 2012;40:D290–301.

[27] Pinotsis N, Chatziefthimiou SD, Berkemeier F, Beuron F, Mavridis IM, Konarev PV, et al. Superhelical architecture of the myosin filament-linking protein myomesin with unusual elastic properties. PLoS Biol 2012;10:e1001261.

[28] Ultsch MH, Wiesmann C, Simmons LC, Henrich J, Yang M, Reilly D, et al. Crystal structures of the neurotrophin-binding domain of TrkA, TrkB and TrkC. J Mol Biol 1999;290:149–59.

[29] Wiesmann C, Ultsch MH, Bass SH, de Vos AM. Crystal structure of nerve growth factor in complex with the ligand-binding domain of the TrkA receptor. Nature 1999;401:184–8.

[30] Banfield MJ, Naylor RL, Robertson AG, Allen SJ, Dawbarn D, Brady RL. Specificity in Trk receptor:neurotrophin

interactions: the crystal structure of TrkB-d5 in complex with neurotrophin-4/5. Structure 2001;9:1191–9.

[31] Bertz M, Wilmanns M, Rief M. The titin-telethonin complex is a directed, superstable molecular bond in the muscle Z-disk. Proc Natl Acad Sci U S A 2009;106:13307–133310.

[32] Vagin A, Teplyakov A. Molecular replacement with MOLREP. Acta Crystallogr D Biol Crystallogr 2010;66:22–5.

[33] Horton JR, Wang H, Mabuchi MY, Zhang X, Roberts RJ, Zheng Y, et al. Modification-dependent restriction endonuclease, MspJI, flips 5-methylcytosine out of the DNA helix. Nucleic Acids Res 2014;42:12092–120101.

[34] Murshudov GN, Skubak P, Lebedev AA, Pannu NS, Steiner RA, Nicholls RA, et al. REFMAC5 for the refinement of macromolecular crystal structures. Acta Crystallogr D Biol Crystallogr 2011;67:355–67.

[35] Bricogne G, Blanc E, Brandl M, Flensburg C, Keller P, Paciorek W, et al. BUSTER version 2.10.0. Cambridge, United Kingdom: Global Phasing Ltd.; 2011.

[36] Zhang Y, Skolnick J. TM-align: a protein structure alignment algorithm based on the TM-score. Nucleic Acids Res 2005; 33:2302–9.

[37] Pronk S, Pall S, Schulz R, Larsson P, Bjelkmar P, Apostolov R, et al. GROMACS 4.5: a high-throughput and highly parallel open source molecular simulation toolkit. Bioinformatics 2013;29:845–54.

[38] Sorin EJ, Pande VS. Exploring the helix–coil transition via all-atom equilibrium ensemble simulations. Biophys J 2005;88: 2472–93.

[39] Fornili A, Pandini A, Lu HC, Fraternali F. Specialized dynamical properties of promiscuous residues revealed by simulated conformational ensembles. J Chem Theory Comput 2013;9:5127–47.

[40] Grove BK, Kurer V, Lehner C, Doetschman TC, Perriard JC, Eppenberger HM. A new 185,000-dalton skeletal muscle protein detected by monoclonal antibodies. J Cell Biol 1984; 98:518–24.

[41] Fukuzawa A, Idowu S, Gautel M. Complete human gene structure of obscurin: implications for isoform generation by differential splicing. J Muscle Res Cell Motil 2005;26:427–34.

[42] Young P, Ehler E, Gautel M. Obscurin, a giant sarcomeric Rho guanine nucleotide exchange factor protein involved in sarcomere assembly. J Cell Biol 2001;154:123–36.